

The UC_{2-x} – Carbon eutectic: A laser heating study



D. Manara^{*}, K. Boboridis, S. Morel, F. De Bruycker

European Commission, Joint Research Centre, Institute for Transuranium Elements (ITU), P.O. Box 2340, 76125 Karlsruhe, Germany

HIGHLIGHTS

- The melting behaviour of nominal $\text{UC}_{2.82}$ has been investigated.
- Temperature evolution of the sample emissivity has been observed.
- Surface carbon segregation in $\text{UC}_{2.82}$ during cooling has been observed.

ARTICLE INFO

Article history:

Received 7 July 2015

Received in revised form

15 August 2015

Accepted 18 August 2015

Available online 20 August 2015

Keywords:

Eutectics

Laser heating

Melting

Radiance spectroscopy

Uranium carbides

Nuclear fuel

ABSTRACT

The UC_{2-x} – carbon eutectic has been studied by laser heating and fast multi-wavelength pyrometry under inert atmosphere.

The study has been carried out on three compositions, two of which close to the phase boundary of the UC_{2-x} – C miscibility gap (with C/U atomic ratios 2 and 2.1), and one, more crucial, with a large excess of carbon ($\text{C/U} = 2.82$). The first two compositions were synthesised by arc-melting. This synthesis method could not be applied to the last composition, which was therefore completed directly by laser irradiation. The U – C – O composition of the samples was checked by using a combustion method in an ELTRA[®] analyser. The eutectic temperature, established to be $2737 \text{ K} \pm 20 \text{ K}$, was used as a radiance reference together with the cubic – tetragonal ($\alpha \rightarrow \beta$) solid state transition, fixed at $2050 \text{ K} \pm 20 \text{ K}$. The normal spectral emissivity of the carbon-rich compounds increases up to 0.7, whereas the value 0.53 was established for pure hypostoichiometric uranium dicarbide at the limit of the eutectic region. This increase is analysed in the light of the demixing of excess carbon, and used for the determination of the liquidus temperature ($3220 \text{ K} \pm 50 \text{ K}$ for $\text{UC}_{2.82}$). Due to fast solid state diffusion, also fostered by the cubic – tetragonal transition, no obvious signs of a lamellar eutectic structure could be observed after quenching to room temperature. The eutectic surface C/UC_{2-x} composition could be qualitatively, but consistently, followed during the cooling process with the help of the recorded radiance spectra. Whereas the external liquid surface is almost entirely constituted by uranium dicarbide, it gets rapidly enriched in demixed carbon upon freezing. Demixed carbon seems to quickly migrate towards the inner bulk during further cooling. At the $\alpha \rightarrow \beta$ transition, uranium dicarbide covers again the almost entire external surface.

© 2015 The Authors. Published by Elsevier B.V. This is an open access article under the CC BY license (<http://creativecommons.org/licenses/by/4.0/>).

1. Introduction

If the higher fissile density constitutes a big advantage of actinide carbides as an alternative nuclear fuel to oxides, the uncertainties mostly linked to metastability and uncontrollable oxygen and nitrogen impurities still represent an obstacle to the fabrication and employment of these materials [1]. Moreover, the metallic thermal conductivity and high melting temperature of

actinide carbides ensures a higher conductivity integral margin to melting for these materials with respect to the traditional UO_2 , $\text{UO}_2\text{–PuO}_2$ and ThO_2 fuels.

This feature, together with the better compatibility with liquid metal coolants of carbides compared to oxides, are further reasons making of them good alternative candidates for high burnup and/or high temperature nuclear fuel.

Uranium carbide was traditionally used as fuel kernel for the US version of pebble bed reactors as opposed to the German version based on uranium dioxide. For the Generation IV nuclear systems, mixed uranium–plutonium carbides (U, Pu) C constitute the primary option for the gas fast reactors (GFR) and UCO is the first

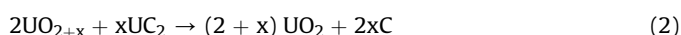
^{*} Corresponding author.

E-mail address: dario.manara@ec.europa.eu (D. Manara).

candidate for the very high temperature reactor (VHTR). In the former case the fuel high actinide density and thermal conductivity are exploited in view of high burnup performance. In the latter, UCO is a good compromise between oxides and carbides both in terms of thermal conductivity and fissile density. However, in the American VHTR design, the fuel is a 3:1 ratio of $\text{UO}_2\text{:UC}_2$ for one essential reason, well explained by Olander [2] in a recent publication. During burnup, pure UO_2 fuel tends to oxidize to UO_{2+x} . UO_{2+x} reacts with the pyrocarbon coating layer according to the equilibrium:



The production of CO constitutes an issue in the VHTR because the carbon monoxide accumulates in the porosity of the buffer layer. The CO pressure in this volume can attain large values and, along with the released fission gas pressure, it can compromise the integrity of the coating layers and contribute to the kernel migration in the fuel particle ("amoeba effect"). In the presence of UC_2 , the following reaction occurs rather than reaction (1) in the hyperstoichiometric oxide fuel:



Because no CO is produced in reaction (2), this latter is more desirable than (1) in view of the fuel integrity. The simultaneous presence of UC_2 and pure carbon in the fuel assembly, however, creates the possibility of further reaction between the dicarbide and pure carbon, conceivably resulting in the formation of a eutectic in case of thermal excursion. The existence of metal carbide-carbon eutectics in metal-carbon binary systems is well known for decades. The U–C system, in particular, has been studied both theoretically and experimentally [3–7]. However, the existence of a UC_{2-x} –C eutectic has been more postulated on the basis of experimental information collected in the immediate vicinity of the $\text{C/U} = 2.00$ composition [1,8] and thermodynamic optimisation of the binary phase diagram [5] than observed in compositions more abundantly enriched in carbon.

A possible reason for such a lack of experimental information can be sought in the phase demixing, hindering homogeneous synthesis of carbides with a large excess of graphite with traditional synthesis methods such as powder metallurgy or arc melting.

In the current work, uranium dicarbide with a large excess of carbon (up to an atomic ratio $\text{C/U} = 2.8$) was obtained by melting uranium dicarbide in a graphite crucible in an induction furnace up to 2800 K under an inert atmosphere. The thus obtained carbide-carbon mixture was then heated beyond 3500 K by laser irradiation, in order to obtain, upon rapid cooling, a homogeneous material. Simultaneous detection of the sample's real temperature by a fast multi-wavelength spectro-pyrometer permitted, for the first time in our knowledge, sound identification of a liquidus temperature, followed by the eutectic/monotectic transition, and, at much lower temperature, the cubic-tetragonal solid-solid phase transition typical of uranium dicarbide. As a comparison, similar thermograms (temperature versus time curves) are presented for the compositions UC_2 and $\text{UC}_{2.1}$. In addition, analysis of the radiance spectra recorded during the thermal cycles yielded *in situ* estimation of the sample surface composition across the various phase transitions.

2. Experimental approach

2.1. Sample preparation and analysis

Uranium dicarbide buttons were prepared by cutting arc melted

and quenched drops without major difficulties [3]. In contrast, homogeneous samples with larger carbon content could hardly be prepared by the same technique due to the large and uncontrollable separation of pure, solid carbon from the melted phase. Carbon-rich samples were rather produced by directly melting up to 2800 K in an induction furnace under oxygen-free, inert gas flux (helium) $\text{UC}_{1.9}$ fragments placed at the bottom of a graphite cylindrical crucible. The crucible's bottom then resulted in a mixture of graphite and eutectic (Fig. 1a). This part was then further homogenised by laser heating it under inert atmosphere (Ar at 0.3 MPa). After fast quenching to room temperature (cooling rates of 10^4 – 10^5 K s^{−1}), the bottom part of the crucible became a reasonably homogeneous eutectic mixture of carbon and uranium dicarbide, with a large excess of carbon with respect to the exact eutectic composition. This latter has been established to be close to $\text{UC}_{2.00}$ [5]. The melted and re-frozen eutectic surface was then cut away from the rest of the crucible (Fig. 1b). Its exact chemical composition was obtained by crushing a small part of it into a fine powder successively measured in the infrared carbon dioxide analyser described below. By repeating several tests, a reproducible composition $\text{C/U} = 2.82 \pm 0.08$ was obtained with such an approach. The melted and re-frozen eutectic disks cut from the cylindrical graphite crucibles were then mounted again in the laser heating sample holder, and laser shot a few more times beyond melting, in order to study more accurately phase transitions occurring during the thermal cycles, and their repeatability over successive thermal cycles.

Two commercial ELTRA[®] analysers combined with a controlled-atmosphere combustion setup were employed to measure, respectively, the carbon and oxygen content of the current samples. The traditional approach is based on the combustion of a sample at high temperature that permits to form gaseous carbon dioxide (CO_2) from either the carbon or the oxygen contained in the specimen, depending on the atmosphere and the crucible material in which the measurement is carried out (Fig. 2). The measurement is then based on the measured IR absorption of the produced CO_2 at a characteristic wavelength (2640 cm^{-1} or $3.79\text{ }\mu\text{m}$) [9].

In order to measure the carbon content, the sample is placed in an Al_2O_3 crucible inside an electrical induction furnace and heated up to 3500 K under a flow of oxygen (99.99% pure). It is assumed that all and only the carbon from the sample reacts with oxygen to produce CO and CO_2 . These gases pass through a system of filters and catalysts to obtain only CO_2 which is measured by IR-absorption spectroscopy. The quantity of CO_2 analysed directly yields the carbon content of the sample.

In the same way, using a graphite crucible inside a resistance furnace and a helium flow, it is possible to measure the oxygen contained in the sample. In this case, it is assumed that all the oxygen contained in the sample reacts with the crucible during heating and forms CO and CO_2 . The final amount of CO_2 is quantitatively determined by IR spectroscopy and, in this case, all the measured CO_2 corresponds to the oxygen content in the sample. Both systems were calibrated with standard materials such as steel and U_3O_8 .

2.2. Laser heating and fast pyrometry setup

Details of the laser-heating setup used in this research have been reported in a previous publication [10], although the technique has been partially modified in the present work. During the shots, a carbide disk was mounted in a sealed autoclave under an inert atmosphere (slightly pressurised argon at 0.3 MPa), in order to minimise high-temperature oxygen contamination of the samples.

Thermograms were measured on samples laser heated beyond melting by a TRUMPF[®] Nd:YAG cw laser radiating at 1064.5 nm, the

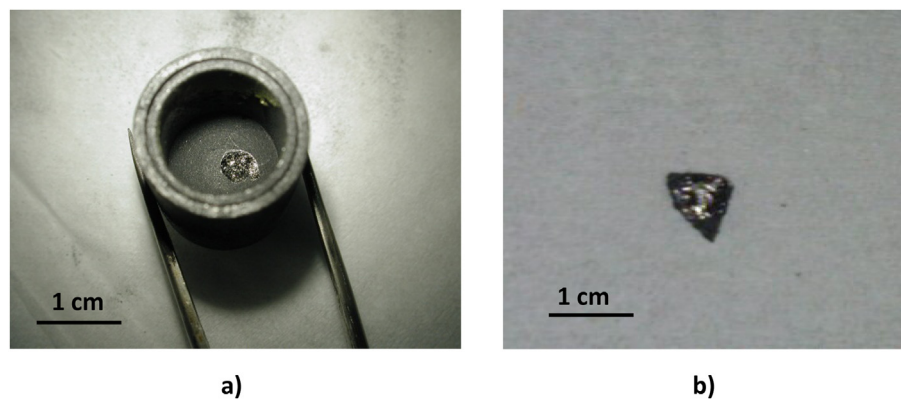


Fig. 1. a) Example of a graphite crucible in which fragments of $UC_{1.9}$ were melted in an induction furnace. The bottom of the crucible is filled with frozen UC – C eutectic. b) Example of melted and re-frozen eutectic surface cut away from the rest of the crucible.

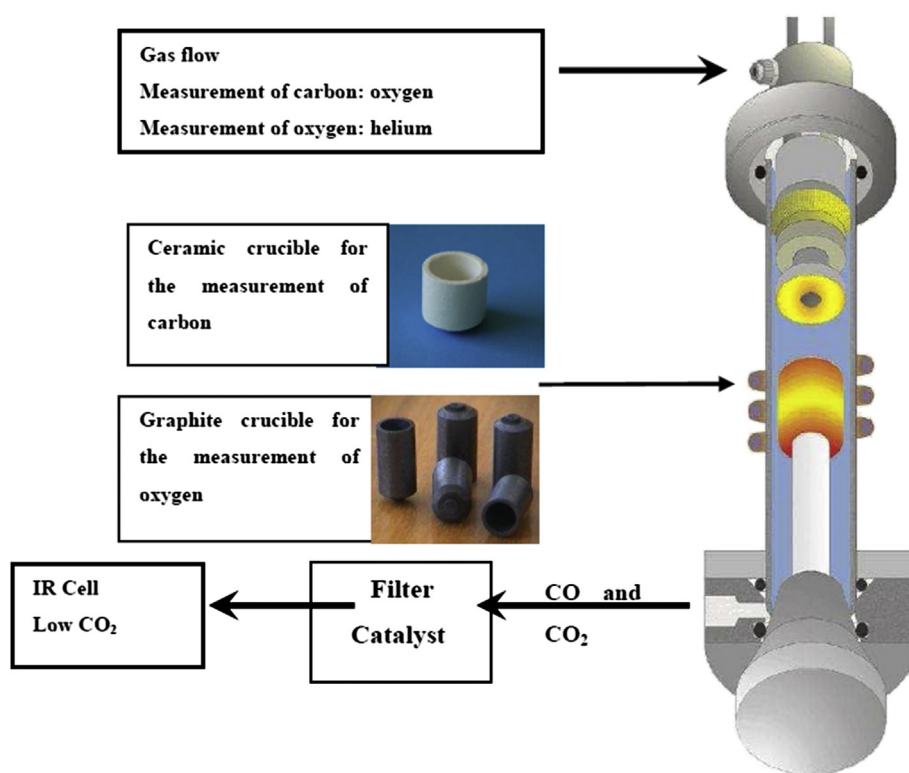


Fig. 2. Schematic of the commercial ELTRA® analyser combined with a controlled-atmosphere combustion setup was employed to measure the carbon and oxygen content of the current samples.

power vs. time profile of which is programmable with a resolution of 1 ms. Pulses of different duration (100 ms–1000 ms) and maximal power (180 W–675 W) were repeated on a 8 mm diameter spot on a single sample surface as well as on different samples of the same composition in order to obtain statistically significant datasets for each composition.

Excessive thermal shocks were minimised by starting each series of laser pulses from a pre-set temperature of about 1500 K. Each series consisted of three heating–cooling pulses on the same sample spot without cooling the material below an intermediate temperature of approximately 1500 K. The peak intensity and duration of the high-power pulses were increased from one heating–cooling cycle to the other, in order to check the result repeatability under slightly different experimental conditions (Fig. 3). This approach constituted a step forward in the laser

heating technique. It ensured a better mechanical stability of the samples, on which several successive shots could be repeated to check the result repeatability and the eventual effects of non-congruent vaporisation or segregation phenomena. The onset of melting was detected by the appearance of vibrations in the signal of a probe laser (Ar^+ cw 750 mW–1.5 W) reflected by the sample surface (reflected Light Signal technique, or RLS) [10]. The sample cooled naturally when the laser beam was switched off during the thermal cycle. Thermal arrests corresponding to exothermic phase transitions were then observed on the thermograms recorded by the fast pyrometers. These operate in the visible–near infrared range between 488 nm and 900 nm. The reference pyrometer wavelength was here 655 nm. This was calibrated according to the procedure already reported elsewhere [6,10].

The normal spectral emissivity (NSE or ϵ_λ) of uranium carbides is

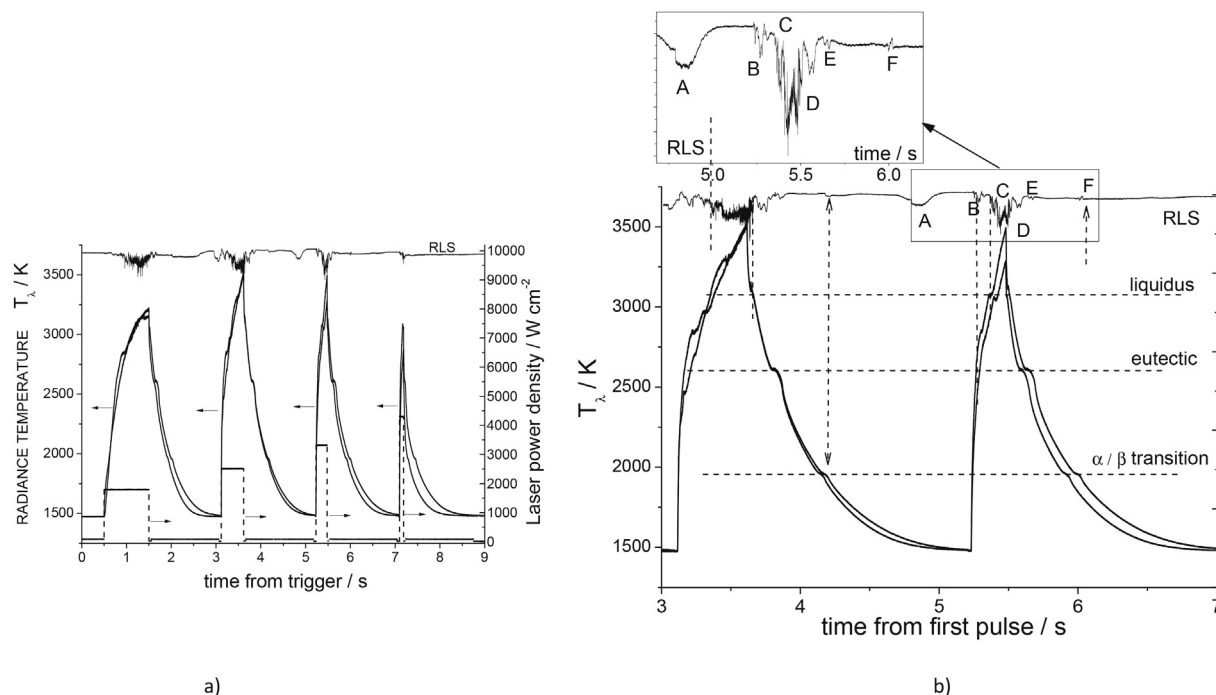


Fig. 3. a) A series of four laser heating/cooling cycles recorded on a UC_{2.82} sample. b) Thermogram details of two heating/cooling cycles, analysed with the help of the reflected light signal (RLS) technique enlarged in the inset. Thermograms are plotted as radiance temperature as a function of time.

necessary for the determination of the sample real temperature T from the radiance temperature T_λ directly measured by the calibrated pyrometers at the wavelength λ , according to the well-known pyrometer equation [11].

$$\frac{1}{T} = \frac{1}{T_\lambda} + \frac{\lambda}{c_2} \ln \varepsilon_\lambda(\lambda, T) \quad (3)$$

Equation (3) is valid within Wien's approximation to Planck's law, i.e. when $\exp\left(\frac{c_2}{\lambda T}\right) > 1$.

If λ is expressed in μm and T in K, then the second radiation constant c_2 takes the value of $14,388 \mu\text{m} \cdot \text{K}$.

NSE of uranium monocarbide UC and uranium dicarbide UC_{2-x} have already been studied in details in recent publications [6]. The normal spectral emissivity of carbon-rich samples has been studied for the first time in this work employing the same multi-wavelength pyrometry approach.

Uncertainty of the temperature measurements was calculated according to the error propagation law [10], taking into account the uncertainty associated to pyrometer calibration, the emissivity, transmittance of the optical system and the accuracy in detecting the onset of vibrations in the RLS signal. The estimated cumulative uncertainty is thus lower than $\pm 1\%$ of the reported temperatures in the worst cases, with a $k = 2$ coverage factor (corresponding to two standard deviations around the average value).

2.3. Pre- and post-melting material characterisation

Characterization of the material composition and its evolution after laser heating/melting has been an essential part of this work. The main techniques employed to this goal are Raman spectroscopy, scanning electron microscopy (SEM), and powder x-ray diffraction (PXRD).

SEM and energy dispersion X-ray spectroscopy (EDX) analyses were performed using a VEGA TESCAN[®] SEM operated at 30 kV and equipped with a SAMx EDS SD-Detector.

PXRD analyses were performed with a Bruker[®] D8 Advance diffractometer (Cu-K α 1 radiation) with a 2θ range of 10° – 120° using 0.009° steps with 2 s of integration time per step at operating conditions of 40 kV and 40 mA. Rietveld analysis of the recorded XRD patterns was performed with the help of the Powder Cell[®] software.

Raman spectra were measured with a Jobin-Yvon[®] T64000 spectrometer used in the single spectrograph configuration. The 647 nm line of a Kr⁺ Coherent[®] laser was used as excitation source, with a nominal power at the laser cavity of 40 mW. This wavelength and power were chosen in order to optimise the signal/noise ratio and reducing undesirable oxidation/burning effects on the sample surface. Spectra were measured in a confocal microscope with a $5 \cdot 10^4$ -fold magnification and long (1 cm) focal distance. With this configuration, the laser power reaching the sample surface was approximately 5 mW. This configuration yielded a good spectral resolution ($\pm 1 \text{ cm}^{-1}$) independently of the surface roughness, with a spatial resolution of $2 \mu\text{m} \times 2 \mu\text{m}$. Eventual polarisation effects on the Raman spectra were neglected in the present investigation. The spectrometer detector angle was calibrated daily with the T_{2g} excitation of a silicon single crystal, set at 520.5 cm^{-1} [12].

3. Results

3.1. Thermogram analysis

Fig. 3a shows two repetitions of four successive heating–cooling cycles recorded on a UC_{2.82} sample. This graph shows that the thermogram shape and thermal arrests are well repeatable from one pulse to the other and even from one set of pulses to the next, even by using laser heating pulses of different intensity and duration. More detailed plots of the two highest power heating pulses well beyond the liquidus temperature are displayed in Fig. 3b. Here some essential phase transitions are better visible on the cooling stage of the thermograms. The same transitions are less clear on the heating flank of the temperature vs. time curves, because of the very fast laser-induced heating. The thermograms reported in Fig. 3a and b

are expressed in radiance temperature T_λ , corresponding to a virtual sample surface $NSE = 1$. Phase transition temperatures reported in Fig. 3a and b will be considerably modified according to equation (3) after the emissivity NSE reassessment discussed in the next section. Three thermal arrests are clearly visible in the thermograms recorded on $UC_{2.82}$ heated well beyond 3000 K (Fig. 3b). Following the U–C phase diagram recently established [5], these can be attributed to the following phase transitions: liquidus temperature, UC_2 –C monotectic, and cubic – tetragonal ($\alpha \rightarrow \beta$) solid transition. The first two transitions can also be identified with the help of the Reflected Light Signal (RLS) curve, displayed in Fig. 3a and b, and zoomed in the inset of Fig. 3b. In particular, six events occurring on the sample surface during a laser heating pulse can be identified in the RLS curve magnified in the inset of Fig. 3b. They are marked in Fig. 3b with the letters from A to F. A reasonable attribution of these events is possible by reading, on the corresponding thermogram, the surface temperatures at which they occur. A transition occurs slightly above 1400 K, where no phase boundaries are expected. It can therefore be explained with the formation of a morphological defect (e.g.: a crack) on the sample surface. B marks the onset of slight oscillations in the RLS. It can be attributed to the formation of the first liquid spots on the surface, i.e. to the solidus transition. C denotes the onset of large oscillations, and indicates complete melting of the surface, corresponding to the liquidus point. Consistently, these large oscillations cease at point D corresponding, within the temperature uncertainty, to the liquidus transition on cooling (formation to the first crystallites in the liquid pool). Likewise, point E (end of the weaker oscillations) indicates total solidification (solidus point). For compositions with excess carbon, this solidus point also corresponds to the UC_{2-x} – C eutectic temperature. Finally, the event marked with F in the RLS curve occurs corresponds, in a repeatable way in the various pulses, to the cubic – tetragonal ($\alpha \rightarrow \beta$) solid state transition of uranium dicarbide. It is interesting to notice that even this solid – solid phase transition implies a slight effect (vibration or morphological change) in the sample surface, visible in the RLS curve. Of course this has an impact on the morphology of the solidified eutectic quenched to room temperature and successively observed by electron microscopy.

The cooling stages of single thermograms relative to the three carbide compositions investigated in this work are reported in Fig. 4.

Only the last two transitions (solidus – eutectic and $\alpha \rightarrow \beta$) are obvious in the thermograms relative to the samples UC_2 and $UC_{2.1}$,

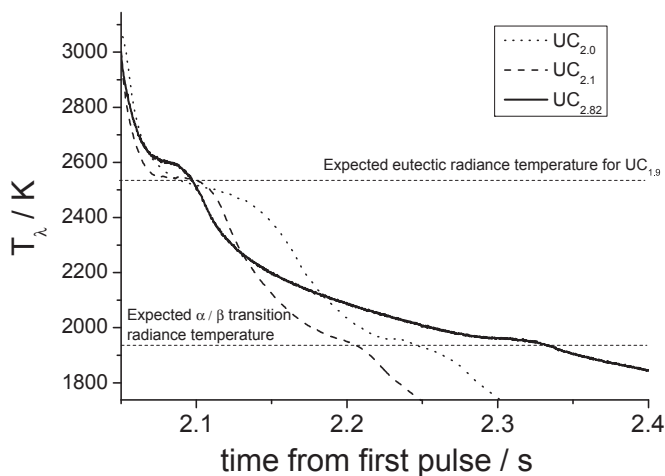


Fig. 4. The cooling stages of single thermograms relative to the three carbide compositions investigated in this work: UC_2 , $UC_{2.1}$ and $UC_{2.82}$. Thermal arrests are visible at the eutectic/monotectic transition and the cubic/tetragonal transition. These transitions appear at higher temperatures in $UC_{2.82}$ probably due to the emissivity effect of excess free carbon.

certainly because the liquidus is too close to the monotectic for the two thermal arrests to be clearly distinguished (at the proposed eutectic composition, $UC_{2.00}$, the two temperatures should actually coincide). It can also be seen that the same phase transitions are visible by thermal arrests at higher radiance temperatures in the sample $UC_{2.82}$. This effect can be attributed to an increase in the sample emissivity linked to the higher carbon content, as already recently observed, for example, in the zirconium – carbon system [14]. The NSE of uranium dicarbide has been established to be 0.53 at $0.655 \mu m$ [6]. If one substitutes this value in equation (3) to obtain real temperature thermograms for UC_2 and $UC_{2.1}$, the relative phase transitions do occur at the temperatures recommended in the literature (2737 K for the eutectic and 2050 K for the $\alpha \rightarrow \beta$ transition). Obviously, higher NSE values should be used for the $UC_{2.82}$ sample. This point will be discussed in section 4.1 of the present paper.

3.2. Radiance spectra

Thermal radiation (Planck) spectra were recorded by multi-wavelength pyrometry at several time points, identified by full circles on the $UC_{2.82}$ thermogram plotted in Fig. 5a. Fig. 5b shows four examples of these spectra recorded at different temperatures. One of them was recorded in liquid $UC_{2.82}$, the other three correspond to the thermal arrests visible in Fig. 5a. Because of a poor signal-to-noise ratio at the tails of the recorded spectra, data were only considered for the current analysis between $0.550 \mu m$ and $0.900 \mu m$. Calling $S_i(\lambda, T)$ be each of these spectra, the following relation holds:

$$S_i(\lambda, T) = \varepsilon_{\lambda i} \cdot P_i(\lambda, T). \quad (4)$$

$P_i(\lambda, T)$ is the Planck (ideal black body) emission function at temperature T :

$$P(\lambda, T) = \frac{c_{1L}}{n^2 \cdot \lambda^5} \cdot \left[\exp\left(\frac{c_2}{n \cdot \lambda \cdot T}\right) - 1 \right]^{-1}. \quad (5)$$

where $c_{1L} = 2 \cdot h \cdot c_0^2$ is the first radiation constant and $c_2 = h \cdot c_0 \cdot k$ is the second radiation constant; c_0 is the speed of light in vacuum, h is Planck's constant, and k_B is the Boltzmann constant already considered in equation (3). For the purposes of the present work, the refractive index was always taken to be equal to 1 (being the current medium air or an inert gas close to atmospheric pressure).

Because uranium carbides are metallic materials (their electronic density of states does not vanish at Fermi level) [1], their NSE cannot be assumed to be wavelength-independent in the investigated spectral range [11]. Under these conditions, it has been shown that direct fit of experimental radiance spectra $S_i(\lambda, T)$ with functions of the type $P(\lambda, T)$ of equation (5) can yield very inaccurate results for ε_λ and T [13]. The problem is inverted by imposing, whenever possible, well-established temperatures for the observed thermal arrests. Equations (4) and (5) permit then direct determination of the normal spectral emissivity $\varepsilon_{\lambda i}$ in the corresponding spectra. This procedure is only possible for spectra $S_i(\lambda, T)$ recorded at the eutectic arrest (2737 K [5]) and at the cubic – tetragonal ($\alpha \rightarrow \beta$) solid state transition of uranium dicarbide, fixed at 2050 K [1]. In these two cases, the sample NSE for each spectrum $S_i(\lambda, T)$ can then be obtained by solving equation (4) for $\varepsilon_{\lambda i}$, i.e. respectively:

$$\varepsilon_{\lambda i}(2737) = \frac{S_i(\lambda, 2737)}{P(\lambda, 2737)}. \quad (6)$$

$$\varepsilon_{\lambda i}(2050) = \frac{S_i(\lambda, 2050)}{P(\lambda, 2050)}. \quad (7)$$

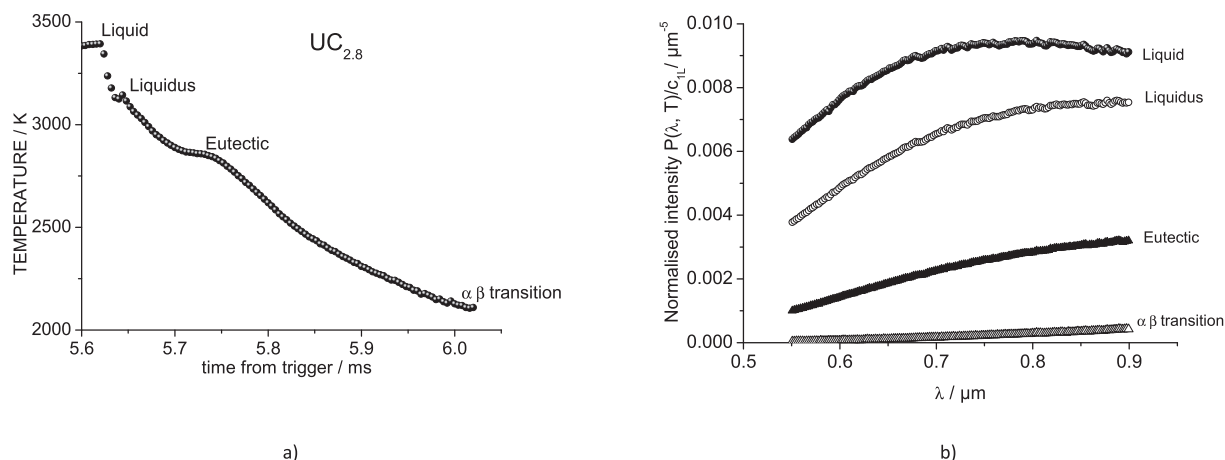


Fig. 5. a) The cooling stage of a thermogram recorded on a $UC_{2.82}$ sample. Full circles identify the time points at which $S_i(\lambda, T)$ spectra were recorded by multi-wavelength pyrometry. b) Four examples of $S_i(\lambda, T)$ spectra recorded at different temperatures. One of them was recorded in liquid $UC_{2.82}$, the other three correspond to the thermal arrests in Fig. 5a.

It should be noted, incidentally, that imposing the eutectic–monotectic temperature at any composition between $UC_{1.9}$ and pure C implies the assumption of zero uranium dicarbide solubility in pure graphite. Such assumption is certainly reasonable when one considers the very different structures of the two phases.

The trends thus obtained for ε_λ in $UC_{2.82}$ at the eutectic and the cubic–tetragonal transition temperatures are reported in Fig. 6. The reported uncertainty bands are calculated considering the intrinsic uncertainty of the radiance spectra measurements, and the uncertainty affecting the assumed reference temperatures ($2737\text{ K} \pm 20\text{ K}$ and $2050\text{ K} \pm 20\text{ K}$). The difference between the two NSE average trends gives an idea of the temperature dependence of this parameter. On the other hand, it was shown [6] that the temperature dependence of NSE in UC_2 and pure carbon is smaller than the experimental uncertainty between 2050 K and the uranium carbide melting point. Therefore, one should assume that the variation of NSE reported in Fig. 6 between 2050 K and 2737 K can be due to a real change in the surface composition, as mentioned at the end of subsection 3.1. Obtaining the NSE (ε_λ) of the investigated carbide compositions, and in particular of the high-carbon content sample at different temperatures, becomes then a complex task, requiring a parallel analysis of the thermal radiance and surface composition during the heating/cooling process. This analysis is possible with the current data. It is reported in section 4 of this paper.

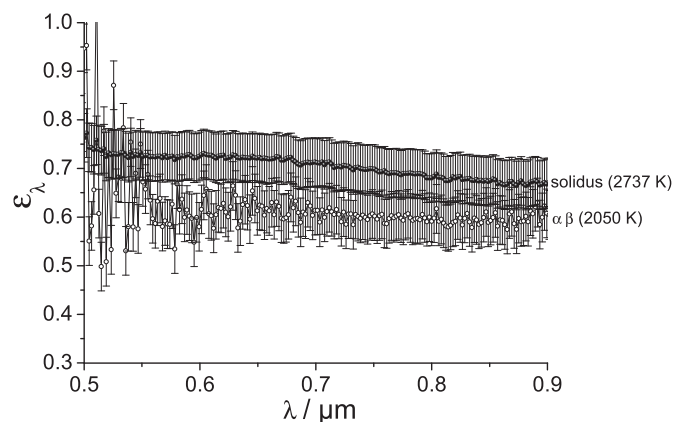


Fig. 6. The trends obtained for ε_λ at the well-established eutectic ($2737\text{ K} \pm 20\text{ K}$) and the cubic–tetragonal ($2050\text{ K} \pm 20\text{ K}$) transition points in $UC_{2.82}$.

3.3. Materials characterisation

As a support to the described radiance spectroscopy analysis, the surface of the current uranium carbide samples has been studied by scanning electron microscopy (SEM) (Fig. 7), PXRD (Fig. 8) and Raman spectroscopy (Fig. 9) after quenching to room temperature.

SEM images in Fig. 7 show that the morphology of eutectic quenched samples is rather irregular. Unlike other metal–carbide systems, no lamellar eutectic structure is recognizable here. Instead, pure carbon is visible on the sample surface in the form of acicular spots. This observation agrees with earlier ones, performed on uranium dicarbide only [8]. Although it is impossible to quantitatively estimate the corresponding carbon surface area fraction s_C , from such tiny acicular spots of carbon, it seems reasonable to assume that it must be very small in these images recorded at room temperature.

PXRD patterns were recorded on powdered samples. Therefore, this cannot be strictly considered as a surface analysis method. Nonetheless, results are useful in clearly identifying two phases in the specimens quenched to room temperature: graphite and tetragonal uranium dicarbide. The XRD pattern of $UC_{2.82}$ is shown in Fig. 8. Patterns of UC_2 and $UC_{2.1}$ are similar, with less intense graphite peaks. This confirms that at lower temperatures the present samples follow the metastable phase boundaries recently assessed for the U–C binary system [14,5]. Because of its extremely slow kinetics [1], the formation of uranium sesquicarbide, U_2C_3 , which would be thermodynamically favourable, is not observed with the current high cooling rates.

Raman spectra recorded on the quenched surfaces of samples laser melted in this work are reported in Fig. 9. From the established emissivity values, and using Kirchhoff's theorem stating that emissivity equals absorptivity at the thermodynamic equilibrium [11], the penetration depth of the current Raman analysis can then be determined to be a few hundred nm. Therefore, the current Raman analysis can be considered to be representative of the sample's external surface, plus a small volume into the bulk material. No Raman active peaks are observed for cubic or tetragonal uranium carbides, by analogy with similar carbides more broadly investigated [16]. A very strong Raman peak is only visible at 1589 cm^{-1} . This is the well-known G peak of graphite. Interestingly, in the quenched eutectic sample this peak is not accompanied by its homologue at 1350 cm^{-1} (the “D peak” of graphite), which is typical of defective and disordered graphite [17]. Both peaks are actually visible in a “clean” graphite crucible identical to those used for the in-furnace synthesis

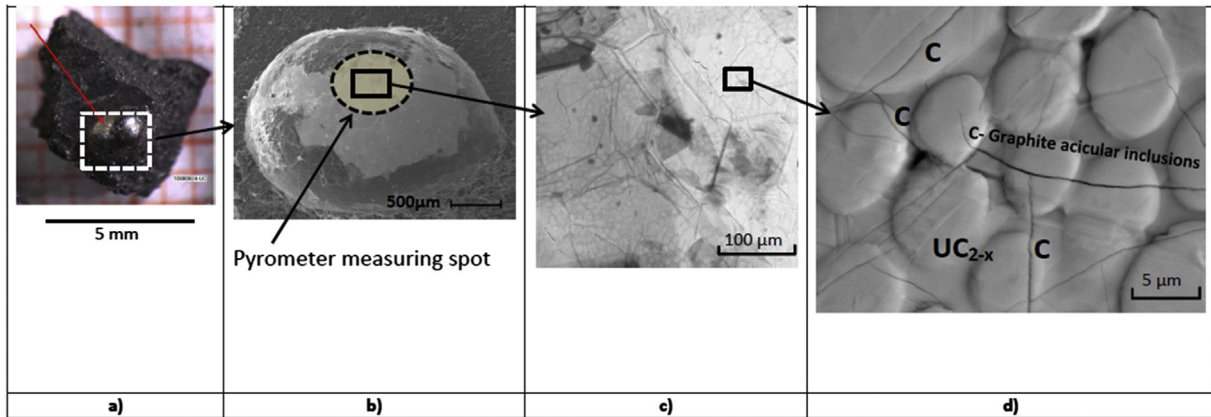


Fig. 7. Optical and Scanning Electron Microscopy images of laser melted and refrozen $UC_{2.82}$. a) Optical overview of a sample after laser irradiation. b) Secondary Electron image of the laser melted and refrozen zone. As already observed in other carbide eutectic systems [14], this quenched zone is swollen, probably due to the large internal strains induced by structures formed in the material upon fast cooling. The circle indicates the approximate measuring spot of the pyrometer. b) and c) More enlarged back-scattered electron (BSE) images of a portion of the melted and refrozen zone inside the pyrometer measuring spot. In the BSE configuration, dark areas are richer in lighter elements. In this case, they correspond to graphite acicular inclusions.

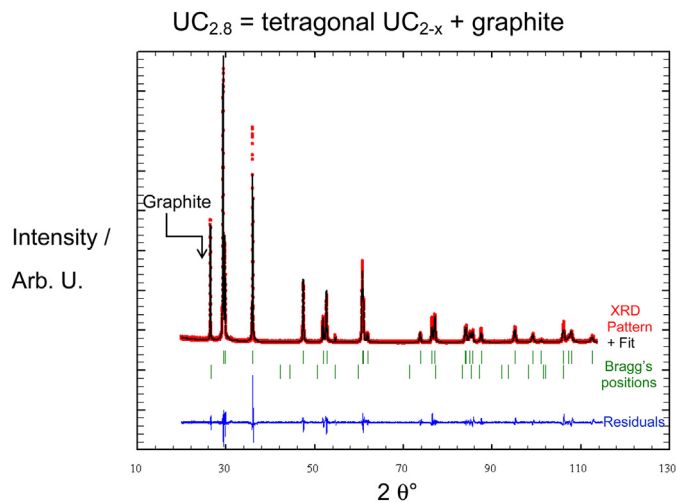


Fig. 8. PXRD pattern recorded on laser melted and refrozen $UC_{2.82}$. Two main phases are visible: tetragonal UC_{2-x} and graphite.

of the current $UC_{2.82}$ samples. Also the G peak appears more complex in the pure graphite sample, where a shoulder (sometimes called “G” [17]) is visible at a slightly higher wavenumber than the main peak. This observations lead to the conclusion that highly ordered graphite is produced in the acicular C-inclusions formed on the quenched surface of the present hyperstoichiometric carbide samples. Similarly ordered graphite was produced by quenching ZrC–C eutectic samples from the liquid phase [14]. This conclusion justifies the choice of the carbon NSE value reported in equation (7). The emissivity of highly ordered graphite has actually been assessed to be very high, approaching 1 [15].

4. Discussion

The present results are the first reported on the melting behaviour of uranium carbides containing a large amount of excess carbon. For their interpretation it is therefore reasonable to refer, by analogy, to similar transition metal-carbide systems the high temperature behaviour of which has been studied more extensively. In particular, the zirconium – carbon eutectic system has been recently investigated with the same approach as the present uranium – carbon system [14].

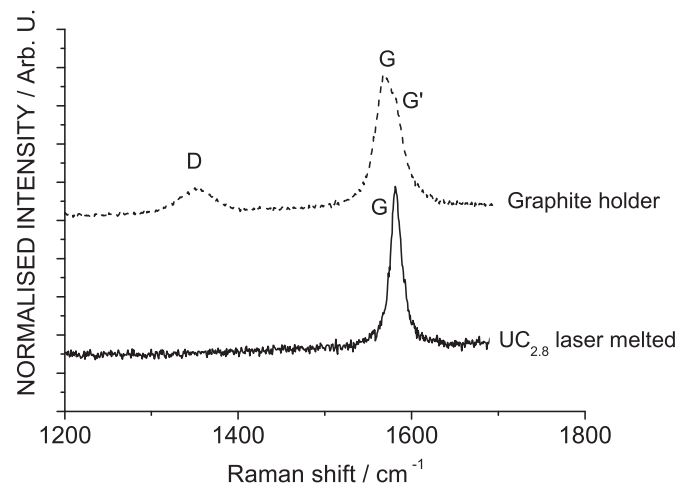


Fig. 9. Raman spectra recorded on molten and refrozen $UC_{2.82}$, compared to the spectrum of the pure graphite used as starting material for the current sample synthesis. The practical absence of a D and G' band in the carbide sample shows that free carbon inclusions in it are constituted by highly ordered graphite.

4.1. Determination of the NSE of melting UC_{2+x} and the liquidus temperature

Estimating the NSE of melting and solidifying UC_{2+x} from the radiance spectra of the type of those reported in Fig. 5b constitutes a first, complex task. It is necessary, however, for the determination, through equation (3), of the real liquidus temperature of the observed composition. Two main difficulties need to be faced: 1) The investigated material surface is a composite one, mixture of two immiscible phases (uranium dicarbide and graphite) having different optical properties; 2) NSE cannot be rigorously assumed to be wavelength-independent in this type of carbides.

It has been observed in the Zr–C system [14], that the presence of excess carbon not soluble in the carbide matrix results, both in the liquid and upon eutectic solidification, in an increased NSE with respect to the metal carbide at the limit of the eutectic domain. This effect has been explained on the basis of the definition of NSE and Planck's radiation law, as in equation (5), taking into account the area fraction of carbon with respect to the carbide matrix in the quenched solid eutectic surface. The following equation can be easily derived for the total NSE of the composite surface:

$$\varepsilon_{\lambda TOT} = \varepsilon_{\lambda UC2-x} \cdot S_{UC2-x} + \varepsilon_{\lambda C} \cdot S_C \quad (8)$$

Here $\varepsilon_{\lambda UC2-x}$ is the NSE of uranium dicarbide, $\varepsilon_{\lambda C}$ the NSE of pure carbon, S_{UC2-x} and S_C are the surface area fractions of UC_{2-x} and C, respectively ($0 \leq S_{UC2-x}, S_C \leq 1$, $S_{UC2-x} + S_C = 1$). The total NSE of the composite surface, $\varepsilon_{\lambda TOT}$, is obtained here from the current experimental results with the help of equations (4) and (5). Obviously, here $\varepsilon_{\lambda TOT}$ coincides with $\varepsilon_{\lambda i}$ of equation (4).

It is worth specifying, at this point, that “surface composition” means here the average composition of the external layer of material, from which is mostly emitted the thermal radiation detected by the current multi-wavelength pyrometer. The lack of refractive index data for cubic uranium dicarbide [1] and the fact that the present material is actually biphasic, make it impossible to provide any accurate determination of the thickness of such a layer. However, taking into account the wavelength range investigated in the present analysis, the numerical aperture of the pyrometer objective and arbitrary values for the complex refractive index compatible with the current emissivity data, an approximate penetration depth of 100 nm–200 nm can be estimated for the present thermal radiance emission analysis. Such penetration depth corresponds to the thickness of the surface layer investigated in this work.

The differences between the $UC_{2.82}$ NSEs at the eutectic and $\alpha \rightarrow \beta$ transition temperatures shown in Fig. 6 are likely to depend on the surface morphology and composition evolution during cooling, according to equation (8). In fact, the NSE trends of Fig. 6 are successfully fitted with the help of equation (8), assuming the following expressions for $\varepsilon_{\lambda UC2-x}$ and $\varepsilon_{\lambda C}$:

$$\varepsilon_{\lambda UC2-x} = 0.75 - 0.42 \cdot \lambda + 0.18 \cdot \lambda^2 \quad (9)$$

$$\varepsilon_{\lambda C} = 0.96 \pm 0.03 \text{ (SOLID)}. \quad (10)$$

Equation (9) was proposed in an experimental assessment of optical properties of melting and solid uranium carbides [6], whereas equation (10) is deduced from a recent review [15], and is reasonable for highly ordered solid graphite. The fit yields different values of the sample surface composition at the two temperatures: $S_C = 0.3$ at the eutectic point and S_C close to zero at the cubic–tetragonal transition point. Of course, these results are affected by an uncertainty even larger than the one reported for the NSE values. Nonetheless, this procedure, applied at particular temperatures for which the material behaviour is relatively well-established, shows that even for the carbon-rich compositions it is reasonable to use the NSE values and trends recommended for uranium dicarbide and specimens with little excess carbon. With this assumption, the approach can then be extended to all temperatures, and spectra $S_i(\lambda, T)$ can be fitted using temperature and S_C as free parameters, instead of T and ε_{λ} . For radiance spectra measured in the liquid, the following value for the NSE of pure liquid carbon is taken:

$$\varepsilon_{\lambda CL} = 0.87 \pm 0.05 \text{ (LIQUID)}, \quad (11)$$

as recently extrapolated for the system ZrC–C [14].

By combining equations (4), (5) and (8) one obtains the following fitting equation:

$$P(\lambda, T) = \frac{c_{1L}}{\lambda^5} \cdot \frac{1}{\exp\left(\frac{c_{2L}}{\lambda \cdot T}\right) - 1} \cdot (\varepsilon_{\lambda UC2} + (\varepsilon_{\lambda C} - \varepsilon_{\lambda UC2})S_C) \quad (12)$$

Using equations (9)–(11) for the various emissivity expressions, the fit yields the best values of the real temperature T and the carbon surface area fraction S_C for each radiance spectrum recorded. Fig. 10 reports, for sample $UC_{2.82}$, the resulting temperature and total NSE given by equation (8) once S_C is determined with the

described procedure. Finally, considering the uncertainty propagation through the whole fitting procedure, and the large cooling rate compared to the acquisition time of radiance spectra (4 ms), the $UC_{2.82}$ liquidus temperature, corresponding to the first thermal arrest observed in the thermograms of Fig. 3, can be determined only with a large error band: $T_{liquidus}(UC_{2.82}) = 3220 \text{ K} \pm 50 \text{ K}$.

In conclusion, the segregation of a pure carbon phase on the sample surface during the heating/cooling cycles plays an important role in the radiative heat transfer balance of this type of carbides. The corresponding evolution of the surface composition resulting from current radiance spectra fit is discussed in the next section.

4.2. Evolution of the sample surface composition during cooling and after room temperature quenching

As a summary of the present study, Fig. 11 reports the trend of the C/U atomic ratio on the surface of a $UC_{2.82}$ sample, between 2000 K and 3500 K. The C/U ratio has been obtained by assuming, according to the present room temperature PXRD results combined with literature data up to 2500 K [1], that the uranium dicarbide phase in equilibrium with pure carbon at the limit of the eutectic region has the composition recommended in Ref. [1]. Then the C/U atomic ratio can be written:

$$C/U = f(T) + s_C(T), \quad (13)$$

Where $s_C(T)$ is obtained by fitting the current radiance spectra with equation (12). The term $f(T)$ represents, as a function of temperature, the C/U ratio at which uranium dicarbide is in equilibrium with pure graphite. Using the phase boundaries reported in Refs. [4] and [5], it can be approximated by the following linear relationship:

$$f(T) = 1.89 + 4.4 \cdot 10^{-5} \cdot T \quad (14)$$

for $2050 \text{ K} \leq T \leq 2737 \text{ K}$.

Carbon enrichment on the sample surface is always significantly lower than the excess carbon content of the initial bulk composition. This can be explained at all temperatures with a higher surface tension of uranium dicarbide compared with pure carbon. Only at temperatures where liquid UC_{2+x} and solid C coexist (between solidus and liquidus) and close to solidification a significant excess of carbon can be clearly observed. Obviously, the highly non-congruent solid–liquid transition results in the segregation of solid carbon even on the sample surface. It is not impossible, if the present system follows the conventional eutectic solidification

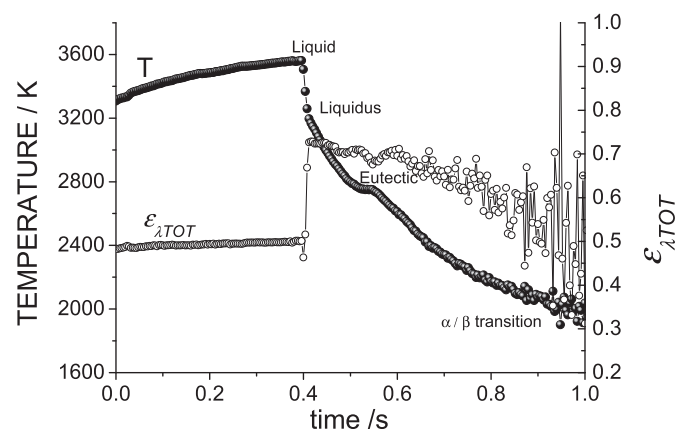


Fig. 10. Temperature and normal spectral emissivity (NSE or ε_{λ}) obtained by fitting the current radiance spectra in $UC_{2.82}$.

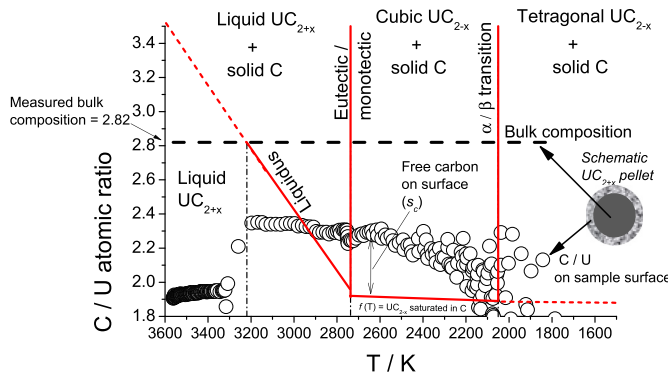


Fig. 11. Empty circles: temperature evolution of the C/U atomic ratio on the surface of a $UC_{2.82}$ sample during the cooling part of a laser heating cycle, compared with the measured bulk sample composition $C/U = 2.82$, plotted as a thick dotted line. Thick red lines indicate the phase boundaries. Experimental surface composition data below 2100 K are scattered because of poor signal/noise ratio in the multi-wavelength pyrometer (For interpretation of the references to colour in this figure legend, the reader is referred to the web version of this article.).

dynamics [18–20], that such solid carbon forms some typical lamellar structures at temperatures immediately lower than the solidification point. However, because of relatively fast carbon diffusion in uranium dicarbide [1], and the thermodynamic force represented by the higher surface tension of UC_{2-x} , these lamellae rapidly dissolve into the bulk, leaving on the surface only those traces similar to acicular spots of highly ordered graphite shown by SEM analysis in Fig. 7 and analysed here by Raman spectroscopy.

Such approximate description of the surface morphology evolution should obviously be corroborated by further experimental characterisation and by calculations of solidification dynamics and solid-state diffusion, which are beyond the scopes of the present work.

Nonetheless it should be appreciated that the current high temperature radiance spectra measurements, combined with some more traditional characterisation techniques on materials quenched to room temperature, permit a consistent analysis of the sample phase transitions and surface features (composition and morphology). At the temperatures studied here ($T > 2500$ K), such features would be hardly accessible, even very qualitatively, to most of the material characterisation techniques available up to date.

Finally, the present results give hints about the possible melting behaviour of uranium carbide nuclear fuel coated in graphite (cf. [21]). Although melting of such type of fuel is very unlikely, even in a reactor mishap, the formation of liquid might indeed result in the migration of the carbide fuel towards the outer surface of the coating. Such information is certainly relevant to the safety analysis of this type of nuclear fuel in accidental conditions.

5. Conclusions

The eutectic system uranium dicarbide-carbon has been studied by laser heating, with particular focus on the composition $UC_{2.82}$, synthesized by melting fragments of uranium dicarbide in a graphite crucible.

The following conclusions can be drawn:

1. The normal spectral emissivity, and, therefore, the thermal radiance emitted by hyperstoichiometric uranium carbides depends on the surface area fraction of free carbon. In particular, NSE of $UC_{2.82}$ reaches a maximum value of 0.7 at the first solidification (liquidus) temperature, compared to the value $NSE = 0.53$ established for pure uranium dicarbide.

2. Accordingly, using as a reference temperature the uranium dicarbide-carbon eutectic, fixed at 2737 K, the liquidus temperature of $UC_{2.82}$ has been measured to be $3220 \text{ K} \pm 50 \text{ K}$.
3. The current radiance spectroscopy measurements permit a qualitative determination of the evolution of the sample surface composition during the heating/cooling process. The surface fraction of carbon, in particular, has always been observed to be considerably lower than the nominal material composition, both in the solid and in the liquid phases. This signifies that uranium dicarbide has probably a higher surface tension than carbon, and that carbon can quickly diffuse into uranium dicarbide, both liquid and solid.
4. As a result, no lamellar eutectic structure has been observed after quenching to room temperature. Instead, a pure graphite phase is demixed in the form of tiny acicular inclusions.
5. Raman spectroscopy measurements have shown that these acicular inclusions consist of highly-ordered graphite.

These results are useful for determining the interaction between uranium dicarbide and carbon in certain so-called “advanced fuel” concepts. The analysis can be extended to other C/U atomic ratios, or to other even less-studied analogous systems, such as, for example, the binary plutonium-carbon.

Acknowledgements

The Authors wish to acknowledge R.J.M. Konings (TU Delft and JRC ITU) for useful scientific discussions, D. Bouexière and R. Eloiirdi (JRC-ITU) for their help in XRD analysis and M. Ernstberger (JRC-ITU) for SEM imaging.

References

- [1] D. Manara, F. De Bruycker, A.K. Sengupta, R. Agarwal, H.S. Kamath, Thermodynamic and thermophysical properties of the actinide carbides, in: R.J.M. Konings (Ed.), *Comprehensive Nuclear Materials*, Elsevier, Amsterdam, 2012.
- [2] D. Olander, *J. Nucl. Mater.* 389 (2009) 1.
- [3] C.A. Utton, F. De Bruycker, K. Boboridis, R. Jardin, H. Noel, C. Guéneau, D. Manara, *J. Nucl. Mater.* 385 (2009) 443.
- [4] E. Fischer, *CALPHAD* 32 (2008) 371.
- [5] C. Guéneau, N. Dupin, B. Sundman, C. Martial, J.-C. Dumas, S. Gossé, S. Chatain, F. De Bruycker, D. Manara, R.J.M. Konings, *J. Nucl. Mater.* 419 (2011) 145.
- [6] D. Manara, F. De Bruycker, K. Boboridis, O. Tougaït, R. Eloiirdi, M. Malki, *J. Nucl. Mater.* 426 (2012) 126.
- [7] G. Raveu, G. Martin, O. Fiquet, P. Garcia, G. Carlot, H. Palancher, A. Bonnin, H. Khodja, C. Raepsaet, T. Sauvage, M.-F. Barthe, *Nucl. Instr. Methods Phys. Res. B* 341 (2014) 72.
- [8] R. Benz, *J. Nucl. Mater.* 31 (1969) 93.
- [9] David R. Lide (Ed.), *CRC Handbook of Chemistry and Physics*, 82nd ed., CRC Press LLC, New York, 2001, pp. 9–19.
- [10] D. Manara, M. Sheindlin, W. Heinz, C. Ronchi, *Rev. Sci. Instrum.* 79 (2008) 113901.
- [11] D.P. DeWitt, J.C. Richmond, Thermal radiative properties of materials, in: D.P. DeWitt, G.D. Nutter (Eds.), *Theory and Practice of Radiation Thermometry*, Wiley, New York, 1988.
- [12] J.H. Parker Jr., D.W. Feldman, M. Ashkin, *Phys. Rev.* 155 (1967) 712.
- [13] G. Neuer, L. Fiessler, M. Groll, E. Schreiber, in: J.F. Schooley (Ed.), *Temperature: its Measurement and Control in Science and Industry*, vol. 6, AIP, New York, 1992, p. 787.
- [14] D. Manara, H.F. Jackson, C. Perinetti-Casoni, K. Boboridis, M.J. Welland, L. Luzzi, P.M. Ossi, W.E. Lee, *J. Eur. Ceram. Soc.* 33 (2013) 1349.
- [15] A.I. Savvatimskiy, *Carbon* 43 (2005) 1115.
- [16] H. Wipf, M.V. Klein, W.S. Williams, *Phys. Stat. Sol. (b)* 108 (1981) 489.
- [17] S. Reich, C. Thomsen, *Philos. Trans. R. Soc. Lond.* 362 (2004) 2271.
- [18] A. Findlay, in: A.N. Campbell, N.O. Smith (Eds.), *The Phase Rule and its Applications*, Dover Inc, 1951.
- [19] D.R. Askeland, *The Science and Engineering of Materials*, Chapman & Hall, London, 1996.
- [20] G. Meng, X. Lin, W. Huang, *Mater. Lett.* 62 (2008) 984.
- [21] D. Wongsawaeng, *J. Nucl. Mater.* 396 (2010) 149.